

Abundances, masses, and weak-lensing mass profiles of galaxy clusters as a function of richness and luminosity in Λ CDM cosmologies

Stefan Hilbert^{1,2*} and Simon D. M. White²

¹*Argelander-Institut für Astronomie, Auf dem Hügel 71, 53121 Bonn, Germany*

²*Max-Planck-Institut für Astrophysik, Karl-Schwarzschild-Straße 1, 85741 Garching, Germany*

24 April 2022

ABSTRACT

We test the concordance Λ CDM cosmology by comparing predictions for the mean properties of galaxy clusters to observations. We use high-resolution N -body simulations of cosmic structure formation and semi-analytic models (SAMs) of galaxy formation to compute the abundance, mean density profile, and mass of galaxy clusters as a function of richness and luminosity, and we compare these predictions to observations of clusters in the Sloan Digital Sky Survey (SDSS) maxBCG catalogue. We discuss the scatter in the mass-richness relation, the reconstruction of the cluster mass function from the mass-richness relation, and fits to the weak-lensing cluster mass profiles. The impact of cosmological parameters on the predictions is investigated by comparing results from galaxy models based on the Millennium Simulation (MS) and another WMAP1 simulation to those from a WMAP3 simulation. We find that the simulated weak-lensing mass profiles and the observed profiles of the SDSS maxBCG clusters agree well in shape and amplitude. The mass-richness relations in the simulations are close to the observed relation, with differences $\lesssim 30\%$. The MS and WMAP1 simulations yield cluster abundances similar to those observed, whereas abundances in the WMAP3 simulation are 2–3 times lower. The differences in cluster abundance, mass, and density amplitude between the simulations and the observations can be attributed to differences in the underlying cosmological parameters, in particular the power spectrum normalisation σ_8 . Better agreement between predictions and observations should be reached with a normalisation $0.722 < \sigma_8 < 0.9$ but closer to the upper value, i.e. between the values underlying the two simulation sets.

Key words: galaxies: general – galaxies: clusters: general – large-scale structure of the Universe – gravitational lensing – cosmology: theory – methods: numerical

1 INTRODUCTION

Clusters of galaxies are a powerful probe of astrophysics and cosmology (Voit 2005). For example, the cluster mass function is very sensitive to the cosmic mean matter density, to the initial fluctuation amplitude (Press and Schechter 1974; Frenk et al. 1990; Eke et al. 1996; Sheth and Tormen 1999) and to dark energy dynamics (Bartelmann et al. 2006; Grossi and Springel 2008; Francis et al. 2009). It can be predicted to high accuracy by numerical simulations (Jenkins et al. 2001; Warren et al. 2006; Lukić et al. 2007).

However, the masses of galaxy clusters cannot be observed directly. Thus one either needs to infer the masses of observed clusters from some more directly observable cluster

property, requiring accurate knowledge of the observable-mass relation and its scatter, or one must directly compare observed and predicted cluster abundance as a function of such observables. These include the X-ray luminosity and temperature of the intracluster gas (Borgani et al. 2001; Reiprich and Böhringer 2002; Stanek et al. 2006; Piffaretti and Valdarnini 2008; Vikhlinin et al. 2009), the number and velocity dispersion of the cluster galaxies (Zwicky 1937; Rines et al. 2003; Kochanek et al. 2003; Becker et al. 2007), the number of giant arcs (Bartelmann et al. 1998; Wambsganss et al. 2004; Fedeli et al. 2008), the weak-lensing signal (Tyson et al. 1990; Cypriano et al. 2004; Hoekstra 2007; Johnston et al. 2007; Reyes et al. 2008), and the Sunyaev-Zel’dovich signal induced by the cluster (White et al. 2002; Schulz and White 2003; Bonaldi et al. 2007; Staniszewski et al. 2008).

* shilbert@astro.uni-bonn.de

Predictions for many cluster observables (e.g. the X-ray luminosity or the cluster richness) and for their relation to the cluster mass require modelling of astrophysical processes such as gas cooling and galaxy formation. Although inaccuracies in such astrophysical models are an unpleasant source of uncertainty for cosmological parameter estimation, they mean that comprehensive observations of clusters can be used to constrain cosmological parameters and models for cluster/galaxy evolution simultaneously.

The largest sample of observed galaxy clusters currently available is the maxBCG cluster catalogue (Koester et al. 2007a). This was extracted from the Sloan Digital Sky Survey (SDSS)¹ using maxBCG, an optical cluster-finding algorithm (Koester et al. 2007b). Constraints on the scatter in the velocity dispersion-richness relation and the mass-richness relation of these clusters have been derived from cluster X-ray and galaxy velocity dispersion observations (Becker et al. 2007; Rozo et al. 2008). Weak-lensing measurements of average cluster mass profiles have also been used to calibrate the mass-richness relation, the mass-optical luminosity relation, and mass-to-light ratio profiles of the maxBCG clusters (Sheldon et al. 2007a,b; Johnston et al. 2007; Reyes et al. 2008). These data provide significant constraints on cosmological parameters (Roza et al. 2009).

In this work, we investigate how well physically based models for galaxy formation in a Λ CDM universe can reproduce the observed relations of cluster richness and luminosity to other cluster properties, most notably mass. We also investigate what information on cosmological parameters and galaxy evolution can be obtained by comparing model predictions to observation. We use the Millennium Simulation (Springel et al. 2005) and two smaller N -body simulations of cosmic structure formation (Wang et al. 2008) in conjunction with semi-analytic models of galaxy evolution (De Lucia and Blaizot 2007; Wang et al. 2008) to create mock catalogues of galaxy clusters selected similarly to the maxBCG catalogue. We compute cluster abundances, average cluster masses, and weak-lensing mass profiles as a function of cluster richness and luminosity, and we compare these to observational results for the SDSS maxBCG sample. In addition, we investigate the scatter in the mass-richness relation, and we discuss how well one can recover the cluster mass function and the weak-lensing mass profiles from the richness-binned cluster abundances and mean masses.

The semi-analytic galaxy models used here couple star formation in galaxies to the properties of the evolving dark matter halo distribution in which the galaxies live. The models have been adjusted to be consistent with various observations, e.g. the luminosities, stellar masses, morphologies, gas contents and correlations of galaxies at low redshift, but they have not been tuned to match the properties of rich clusters. The comparison to observation provided here is thus a direct test of these models. This contrasts with halo occupation distribution models Cooray and Sheth (2002), where the galaxy populations of clusters are adjusted to fit observation without considering whether they could have been built up by physical processes within the evolving dark matter distribution.

Our paper is organised as follows. We discuss the N -

Table 1. The cosmological parameters at redshift 0 for the three simulations used in this study. The parameters are: the baryon density Ω_b , the matter density Ω_M , and the energy density of the cosmological constant Ω_Λ (in units of the critical density), the Hubble constant h (in units of $100 \text{ km s}^{-1} \text{ Mpc}^{-1}$), the primordial spectral index n and the normalisation parameter σ_8 for the linear density power spectrum.

	MS & WMAP1	WMAP3
Ω_b	0.045	0.04
Ω_M	0.25	0.226
Ω_Λ	0.75	0.774
h	0.73	0.743
n	1	0.947
σ_8	0.9	0.722

body simulations and galaxy models, as well as our methods for creating the simulated cluster samples from them in Sec. 2. Results for our simulated cluster samples and a comparison to observation are presented in Sec. 3. Our paper concludes with a summary and discussion in Sec. 4.

2 METHODS

We use cosmological N -body simulations to analyse the matter distribution in and around galaxy clusters in two different Λ CDM cosmologies. We infer the properties of the galaxies in the clusters from model galaxy catalogues generated by applying semi-analytic galaxy formation models to halo assembly trees generated from the outputs of the N -body simulations. We then compute richness and luminosity estimates for clusters in the model galaxy catalogues taking into account several observational features of optical cluster-finding algorithms, in particular maxBCG by Koester et al. (2007b).

2.1 The N -body simulations

Our study is based on three different N -body simulations: the Millennium Simulation (MS) by Springel et al. (2005), and two smaller simulations WMAP1 and WMAP3 by Wang et al. (2008).² The simulations assume a flat Λ CDM cosmology with parameters given in Table 1. Both the MS and the WMAP1 simulation use a parameter set that was derived by combining the WMAP 1st-year results (Spergel et al. 2003) with results from the 2dFGRS Colless et al. (2003). The WMAP3 simulation employs cosmological parameters that are consistent with data from the WMAP 3rd-year release, the Cosmic Background Imager, and the Very Small Array (Spergel et al. 2007), with a bias towards values differing from those used for the other two simulations.

The most prominent differences between the two sets of cosmological parameters are the normalisation parameter σ_8 and the spectral index n for the density power spectrum: The MS and the WMAP1 simulation assume $\sigma_8 = 0.9$ and $n = 1$, whereas the WMAP3 simulation assumes lower values $\sigma_8 = 0.722$ and $n = 0.94$. Hence, there is less power on small scales

¹ <http://www.sdss.org>

² We refer the reader to Springel et al. (2005), Wang et al. (2008), and references therein for more details about the simulations.

Table 2. Numerical parameters for the three simulations used in this study. The parameters are: the comoving cube size L , the particle number n_p , the particle mass m_p , and the effective force softening length ϵ .

	MS	WMAP1	WMAP3
L [h^{-1} Mpc]	500	125	125
n_p	2160 ³	560 ³	560 ³
m_p [$h^{-1}M_\odot$]	8.6×10^8	8.6×10^8	7.8×10^8
ϵ [h^{-1} kpc]	5	5	5

in the matter power spectrum of the WMAP3 simulation than in the MS and the WMAP1 simulation. This results in a substantial delay in structure formation and less massive collapsed structures at any given redshift in the WMAP3 simulation.

The simulations were run using a parallel TreePM version of GADGET2 (Springel 2005). The numerical parameters of the simulations are listed in Table 2. The main difference between the MS and the WMAP simulations is the simulation box size. The 64 times larger volume of the MS provides us with a much larger sample of galaxies and galaxy clusters than the WMAP simulations. The WMAP1 simulation, which shares the cosmological parameters with the MS and the numerical parameters with the WMAP3 simulation, helps us to distinguish the influences of numerical set-up and cosmology on our results.

For each simulation, the particle data were stored on disk at 64 output times. These snapshots contain information on dark-matter halos, which have been identified running a friend-of-friend (FOF) group finding algorithm on the set of simulation particles. The halos were later decomposed into subhalos using SUBFIND (Springel et al. 2001) to identify gravitationally self-bound locally overdense regions. The most massive subhalo, called the main subhalo, typically contains 90% of the FOF halo mass and shares its centre. Detailed merging history trees of all self-bound dark-matter subhalos were then computed. The resulting merger trees were used as input for the semi-analytic models discussed in the following section.

2.2 The semi-analytic galaxy models

We use semi-analytic galaxy formation models from the Munich family (Kauffmann et al. 1999; Springel et al. 2001; De Lucia et al. 2004; Springel et al. 2005; Croton et al. 2006; De Lucia and Blaizot 2007) to set the optical properties of galaxies in the N -body simulations. These semi-analytic models assume that galaxies form from gas that accumulates in the centre of each dark-matter subhalo in the simulation. Star formation in each galaxy is coupled to its subhalo properties via simple prescriptions for gas cooling, star formation, chemical enrichment and feedback from supernova and central black holes (AGNs), as well as for merging of galaxies once their dark matter subhalos have merged. Certain parameters quantifying the efficiency of these processes can be adjusted in order to maximise agreement of the results with observation.

For the MS, we use the publicly available galaxy cata-

logue³ that was generated using the galaxy model described in De Lucia and Blaizot (2007). This MS model reproduces various observed relations for galaxies, in particular the observed luminosity, colour, gas content and morphology distributions (Croton et al. 2006; De Lucia et al. 2006; Kitzbichler and White 2007) and the observed two-point correlation functions (Springel et al. 2005; Kitzbichler and White 2007).

The galaxy model of De Lucia and Blaizot (2007) has been applied by Wang et al. (2008) to the WMAP1 simulation. As expected, this gives similarly good agreement with observations as for the MS. Here, we will use these model galaxies, which we refer to below as the WMAP1-A model, for the WMAP1 simulation.

Wang et al. (2008) also applied the galaxy modelling technique of De Lucia and Blaizot (2007) to the WMAP3 simulation, but with two slightly different sets of efficiency parameters. One, which we call WMAP3-B here, employs the same star formation efficiency as the WMAP1 A model, but lower supernova and AGN feedback efficiencies. The other model, called WMAP3-C in the following, employs a higher star-formation efficiency but also higher feedback efficiencies. Both the WMAP3-B and the WMAP3-C model show good agreement with low-redshift galaxy observations (Wang et al. 2008). In the following, we will consider both models for the WMAP3 simulation.

2.3 The ridgeline galaxies

Optical cluster finding algorithms such as maxBCG (Koester et al. 2007b) locate galaxy clusters by searching for local overdensities of E/S0 ridgeline galaxies in angular and redshift space. These galaxies are common in known clusters, and they are relatively easy to find, since many of them are bright and their observed colours are strongly correlated with luminosity and redshift. Because of their small scatter in colour, a narrow search range in colour can be chosen at each redshift. This narrow search range forces one to know the mean ridgeline colours rather accurately. Accurate mean ridgeline colours are also important for accurately quantifying the ridgeline galaxy content of the clusters.

Although the semi-analytic models can reproduce many of the observed properties of galaxies, there are still some discrepancies. In particular, the population synthesis models they use do not reproduced the colours of passively evolving galaxies to the degree required for a direct application of ridgeline colour-redshift relation used from the maxBCG catalogue. We therefore ‘measure’ the mean ridgeline colours of model galaxies as a function of redshift, fitting a Gaussian with mean \bar{x} and variance σ^2 to the distribution of galaxy colours in a region around the mean ridgeline colour in the colour-magnitude diagram.⁴ The resulting mean ridgeline colours for model galaxies in the MS as a function of redshift is compared to the corresponding relation for SDSS galaxies in maxBCG in Fig. 1.

Following the maxBCG observational procedure, we

³ <http://www.mpa-garching.mpg.de/Millennium>

⁴ The dependence of the mean ridgeline colour on magnitude is ignored, since for all models the slope in the colour-magnitude relation is very small in the considered colours and magnitude range.

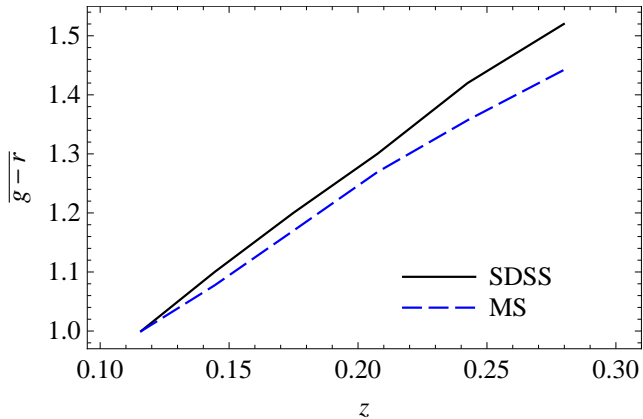


Figure 1. The mean colour $\overline{g-r}(z)$ of the ridgeline galaxies as a function of redshift z for the galaxy model of De Lucia and Blaizot (2007) in the MS compared to the mean colour-redshift relation for the ridgeline galaxies in the SDSS (Koester et al. 2007b).

consider $g-r$ and $r-i$ colours to identify ridgeline galaxies in our simulations. For each simulation snapshot with redshift $0.1 \leq z \leq 0.3$, we select all objects in our semi-analytic galaxy catalogues whose $g-r$ and $r-i$ values are both within 2σ of the mean ridgeline colours. As mean colours, we take the values measured from the simulations. For the ridgeline width σ , we take the observed values $\sigma_{g-r} = 0.05$ and $\sigma_{r-i} = 0.06$ (Koester et al. 2007b).

Besides colour, galaxy brightness is used to select ridgeline galaxies. We thus further select from all model galaxies surviving the colour selection those with apparent observer-frame i -band magnitude $i^{\text{obs}} \leq i_{\text{lim}}^{\text{obs}}$. Here, we employ the same magnitude limit $i_{\text{lim}}^{\text{obs}}$ as Koester et al. (2007b) (B. Koester, private communication). This magnitude limit corresponds to an absolute rest-frame magnitude limit $M_i^{\text{rest}} \approx -20.25 + 5 \log_{10} h \approx -20.9$ for the cosmologies considered here.

2.4 The galaxy clusters

We identify galaxy clusters in the simulations with dark matter halos found by the FOF algorithm. From the simulation data stored on disk, we obtain for each such halo (hence cluster candidate) the positions of the centre, the virial radius $R_{200}^{\text{crit/mean}}$ (i.e. the radius of the largest sphere enclosing $200\times$ the critical/mean density) and the mass $M_{200}^{\text{crit/mean}}$ (i.e. the mass enclosed within $R_{200}^{\text{crit/mean}}$).

The semi-analytic galaxy models provide us with information about the galaxies associated with each dark matter halo. For each halo, we measure the total number $N_{\text{int}}^{\text{gal}}$ of associated ridgeline galaxies selected as described in the preceding section. In addition, we count the number of ridgeline galaxies $N_{1\text{Mpc}}^{\text{gal}}$ within a physical radius of $1h^{-1}$ Mpc in projection along a simulation box axis. The result is used to compute the “observationally defined” radius $R_{200}^{\text{gal}} = 0.156(N_{1\text{Mpc}}^{\text{gal}})^{0.6} h^{-1}$ Mpc (see Hansen et al. 2005; Koester et al. 2007b). We then calculate a scaled galaxy richness N_{200}^{gal} by counting all ridgeline galaxies within a projected radius R_{200}^{gal} . A cluster luminosity L_{200}^{gal} is then computed by summing the i -band luminosities of all ridgeline galaxies within R_{200}^{gal} . These procedures mimic closely those

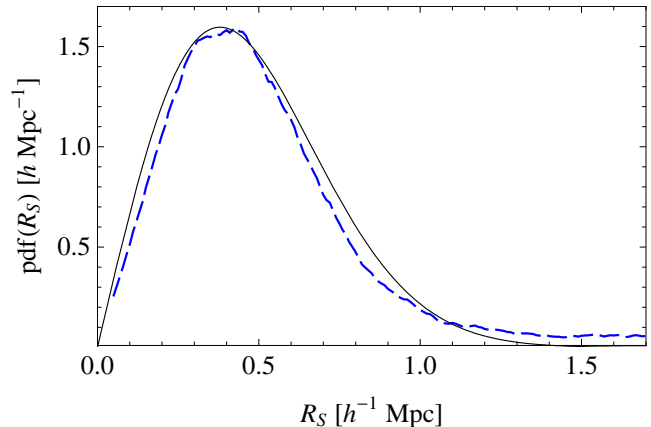


Figure 2. The distribution of projected offset R_s between the ‘true’ and ‘apparent’ centres of miscentred clusters in the MS (dashed line). The distribution is well fit by a 2D Gaussian (solid line).

employed to estimate richnesses and luminosities for the real maxBCG catalogue.

To improve statistics, we perform the measurements of the projected quantities $N_{1\text{Mpc}}^{\text{gal}}$, R_{200}^{gal} , N_{200}^{gal} , and L_{200}^{gal} along all three simulation box axes. Each projection is treated as an individual cluster in the subsequent analysis. For the computation of cluster densities, the resulting triplication of clusters is taken into account by assuming a three times larger simulation volume.

Several effects hamper a direct comparison between observed clusters and our simulated clusters at the stage described so far. Here, we will not take into account fragmentation, but we do correct for contamination of the observational data by foreground and background galaxies.⁵ Using spectroscopic data, Koester et al. (2007a) found that roughly 16% of the galaxies identified by maxBCG as cluster ridgeline galaxies are, in fact, projections. We include such projections in our simulated clusters in a very simple way, by randomly duplicating about 19% of the ridgeline galaxies. As a result, our model clusters appear to be contaminated at the 16% level.

We also consider the effect of misidentifying the cluster centre. For each cluster in the simulations, we calculate galaxy numbers, radii, etc. not only using the ‘true’ centre, but also using the position of the second-most massive subhalo as ‘apparent’ centre. The resulting distribution of projected offsets R_s between ‘true’ and ‘apparent’ centre is shown in Fig. 2 for the MS. The distribution can be approximated by a two-dimensional Gaussian distribution with

$$\text{pdf}(R_s) = \frac{R_s}{\sigma_s^2} \exp\left(-\frac{R_s^2}{2\sigma_s^2}\right) \quad (1)$$

and $\sigma_s = 0.38h^{-1}\text{Mpc}$, which agrees well with the offset distribution found for the maxBCG algorithm run on simulated data (Johnston et al. 2007). We find a similar value,

⁵ Fragmentation is insignificant in the maxBCG sample, but overmerging slightly boosts the cluster richness estimates mainly due to contamination by foreground and background structures (Koester et al. 2007b).

$\sigma_s = 0.41h^{-1}\text{Mpc}$, for the WMAP1 simulation, and somewhat smaller values, $\sigma_s = 0.34h^{-1}\text{Mpc}$, for the WMAP3 simulation.

When needed for our analysis, we will use a probability

$$\tilde{p}_c(N_{\text{int}}^{\text{gal}}) = \frac{1 + 0.04N_{\text{int}}^{\text{gal}}}{2.2 + 0.05N_{\text{int}}^{\text{gal}}} \quad (2)$$

that a cluster in the simulation with $N_{\text{int}}^{\text{gal}}$ ridgeline galaxies is correctly centred. Empirically, this yields roughly the same probability $p_c(N_{200}^{\text{gal}})$ that a cluster with measured richness N_{200}^{gal} is correctly centred as was found for the maxBCG algorithm by Johnston et al. (2007).

In our simulations, centre misidentification tends to reduce the number N_{200}^{gal} of ridgeline galaxies within R_{200}^{gal} for a given cluster. Consequently, the number density of clusters with N_{200}^{gal} above a given threshold is slightly decreased by centre misidentification. Another consequence of centre misidentification in our simulations is a slightly higher average cluster mass and ridgeline galaxy number $N_{\text{int}}^{\text{gal}}$ for a given measured richness N_{200}^{gal} . All these effects may be smaller for the actual maxBCG algorithm. This algorithm disfavours identifying the cluster centre with galaxies that lead to low N_{200}^{gal} in comparison to galaxies that yield a larger cluster richness. In the following, we will thus discuss results for our simulated cluster samples in the case that centre misidentification is ignored, unless stated otherwise.

2.5 The cluster samples

A comparison of cluster abundances in our simulated cluster samples to observation requires knowledge of the volumes and areas of the real surveys. For the SDSS maxBCG cluster sample, we assume an effective survey area of 7400 deg^2 and a redshift range of $0.1 \leq z \leq 0.3$ (Roza et al. 2009). This yields an effective survey volume of $4.3 \times 10^8 h^{-3}\text{ Mpc}^3$ for the MS and WMAP1 cosmology, and $4.4 \times 10^8 h^{-3}\text{ Mpc}^3$ for the WMAP3 cosmology.

For each snapshot of our simulations with redshift $0.1 \leq z \leq 0.3$, we create a model cluster catalogue containing the projections of all clusters in the simulation box. We calculate the statistical properties of interest (e.g. the cluster densities or average cluster mass as a function of cluster richness) for each of these snapshot catalogues (properly taking into account the increased cluster number due to inclusion of multiple projections of each cluster). We then compute the properties of a cluster sample in a volume-limited survey with $0.1 \leq z \leq 0.3$ by an average over the snapshot results, where each snapshot is weighted by its cluster abundance and its volume fraction in the survey.

3 RESULTS

Here, we compare the properties of clusters in our various galaxy formation models to the observed properties of clusters in the SDSS maxBCG catalogue. We investigate average cluster properties as a function of galaxy content by dividing our simulated cluster samples into bins of richness N_{200}^{gal} and luminosity L_{200}^{gal} (as was done for the maxBCG cluster sample). The average properties of the model clusters binned by N_{200}^{gal} are listed for the different galaxy formation models in

Tables 7-10. The properties of model clusters when binned by L_{200}^{gal} are shown in Tables 11-14.

We first present results for stacked weak-lensing mass profiles and for the abundance of clusters, both as a function of galaxy richness. We then discuss the mean and scatter of cluster mass as functions of richness and luminosity. Finally, we study how well the cluster mass function and the stacked weak-lensing mass profiles can be reconstructed from the cluster abundance together with the mean and scatter of the mass-richness relation.

3.1 Cluster mass profiles

For each cluster in the simulations, we compute weak-lensing mass profiles by projecting the simulation particles and the galaxies in a cuboid region of $35h^{-1}\text{ Mpc}$ transverse physical side length and $100h^{-1}\text{ Mpc}$ comoving thickness centred on the cluster. The projected particles and galaxies (assumed to contribute their stellar mass as points)⁶ are binned in annuli to compute the circularly averaged surface mass density $\Sigma(R)$ at radius R from the projected cluster centre, the mean enclosed surface mass density $\bar{\Sigma}(R)$ inside R , and the weak-lensing mass profile

$$\Delta\Sigma(R) = \bar{\Sigma}(R) - \Sigma(R). \quad (3)$$

The weak-lensing mass profile $\Delta\Sigma(R)$ is proportional to the average tangential shear $\langle\gamma_t\rangle(R)$ around the projected cluster centre, and can therefore be measured using weak-lensing observations (Schneider et al. 2006). To increase signal-to-noise, the measured tangential shear may be averaged over a sample of clusters. The resulting shear signal can then be converted to an average mass profile for the observed cluster sample.

In this section, the weak-lensing mass profiles of the simulated clusters in each snapshot are averaged in bins of N_{200}^{gal} . The average profiles from each snapshot are then combined with appropriate weights to obtain a mean profile for each N_{200}^{gal} -bin in a volume-limited survey. In doing this, we also take into account the effect of cluster centre misidentification, which has a considerable impact on the average profiles at radii $R < 1h^{-1}\text{ Mpc}$ (see Sec. 3.7).

In Fig. 3, the weak-lensing mass profiles for the simulated clusters in the MS and the WMAP models are compared to the measured profiles of maxBCG clusters in the SDSS (Sheldon et al. 2007a). The simulated and observed profiles agree remarkably well in detailed shape and amplitude. This is strong evidence that our models provide a realistic description not only of the density profile and galaxy content of galaxy clusters, but also of the maxBCG cluster selection and richness measurement.

Differences between the galaxy models and the observations are small but noticeable. The simulated density profiles of the MS tend to be above the observed profiles in the

⁶ Although particles in the simulations represent the total mass in the simulated parts of the universe, we do not compensate for the additional stellar mass, since (i) the mass in stars is very small compared to the total mass in collapsed objects, and (ii) gas physics increases the dark-matter density in the inner part of the halos compared to collisionless simulations (e.g. Barnes and White 1984; Gnedin et al. 2004).

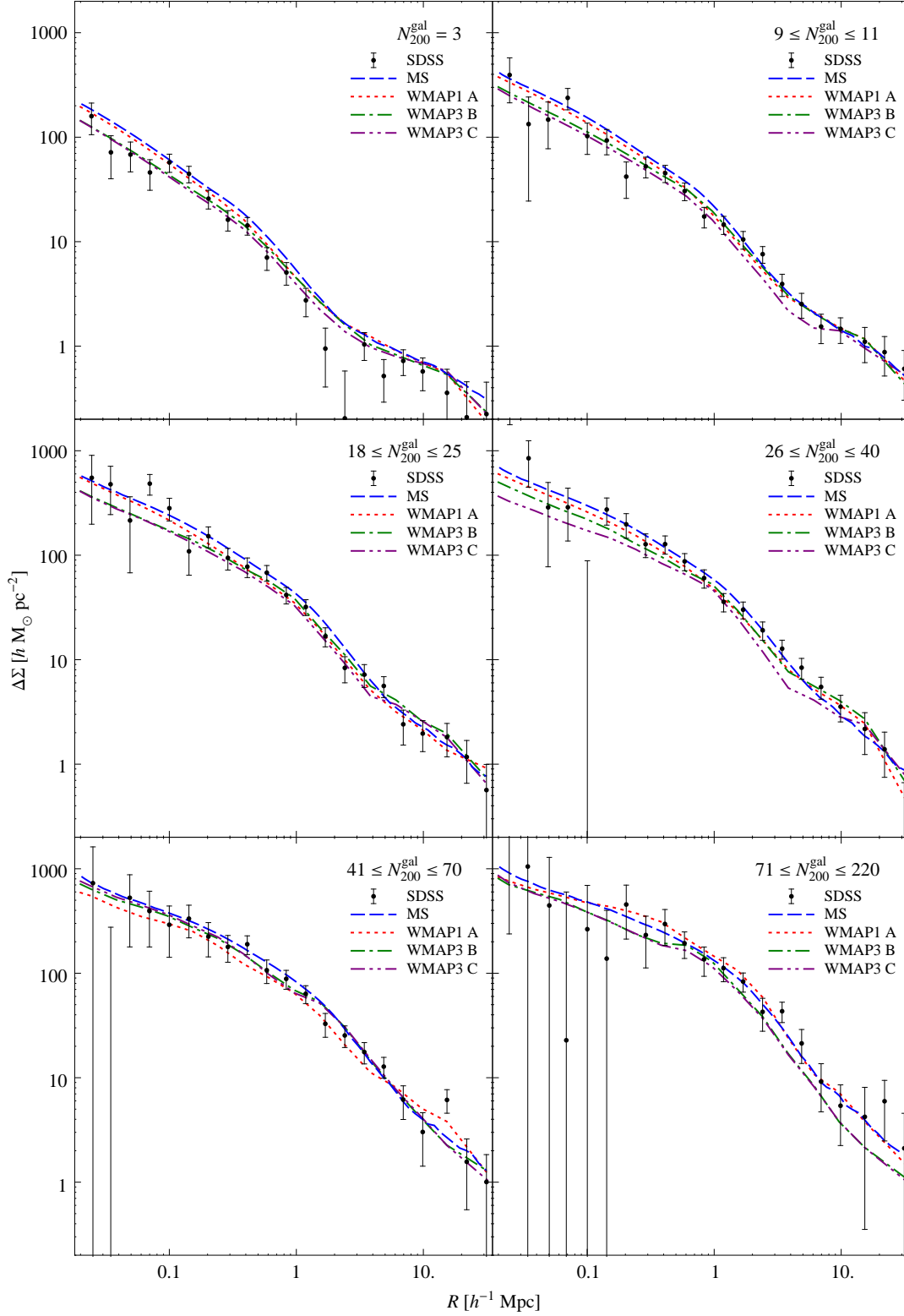


Figure 3. The average weak-lensing mass profile $\Delta\Sigma(R)$ as a function of radius R for clusters in different richness bins in the MS (dashed lines), WMAP1-A (dotted lines), WMAP3-B (dash-dotted lines), and the WMAP3-C model (dash-dot-dotted lines) compared to the observed profiles in the SDSS (points with error bars).

Table 3. The area density $n_{\geq 10}^{\text{ang}}$ [in deg^{-2}] of clusters with richness $N_{200}^{\text{gal}} \geq 10$ and redshift $0.1 \leq z \leq 0.3$ for the model clusters in the MS and WMAP simulations and for the SDSS maxBCG clusters (Koester et al. 2007a). Considered are the cases that all cluster centres are correctly identified ($p_c = 1$), and that only a fraction of clusters given by Eq. 2 is correctly centred ($p_c < 1$).

	$p_c = 1$	$p_c < 1$
SDSS		1.8
MS	1.7	1.4
WMAP1-A	1.8	1.6
WMAP3-B	0.6	0.5
WMAP3-C	0.9	0.7

poorer clusters but are an excellent fit in the rich systems. The WMAP3 model profiles fit better in the poor clusters but are mostly below the observed profiles in richer clusters. For radii $R \lesssim 1h^{-1}\text{Mpc}$, the mass profiles of the WMAP3 models are roughly 30% lower than in the MS/WMAP1 models. This suggests that for given richness, the maxBCG clusters are on average slightly less massive than clusters in the MS/WMAP1 simulations but slightly more massive than those in the WMAP3 simulations. We will investigate this issue in more detail in Sec. 3.3.

3.2 Cluster abundance

Table 3 compares the area density $n_{\geq 10}^{\text{ang}}$ of clusters with richness $N_{200}^{\text{gal}} \geq 10$ and redshift $0.1 \leq z \leq 0.3$ in our simulated surveys to the observed abundance of maxBCG clusters in the SDSS. If we ignore misidentification of the cluster centres, the MS and the WMAP1-A model yield cluster abundances very similar to the real maxBCG cluster sample. In contrast, the cluster abundances for the WMAP3 models are a factor 2-3 lower than that observed in the SDSS. The lowest abundance is found for the WMAP3-B model. Taking into account centre misidentification in our simulations reduces the cluster abundances by $\approx 20\%$ and thus increases the discrepancy between the WMAP3 models and the SDSS cluster sample. The abundance is then also somewhat low even in the MS case, suggesting, as noted above, that our procedure for modelling the effects of centre misidentification may overestimate the effect in the real maxBCG catalogues.

The redshift dependence of the comoving cluster abundance is shown in Fig. 4. All our models show a slight decrease of the comoving cluster density with increasing redshift. For $z > 0.15$, the abundance in the MS and WMAP1-A model agree very well with the maxBCG results. In contrast, there is a much larger observed density at low redshifts $z < 0.15$, which is not seen in the models and presumably reflects nearby large-scale structure such as the SDSS Great Wall.

The dependence of the cluster counts on richness N_{200}^{gal} is illustrated in Fig. 5. Cluster abundances in the MS and WMAP1-A models are lower than in the SDSS for $N_{200}^{\text{gal}} < 20$, but exceed the observed abundances for $N_{200}^{\text{gal}} \geq 20$. Abundances in the WMAP3 models are always lower than in the MS and WMAP1-A model and below the observa-

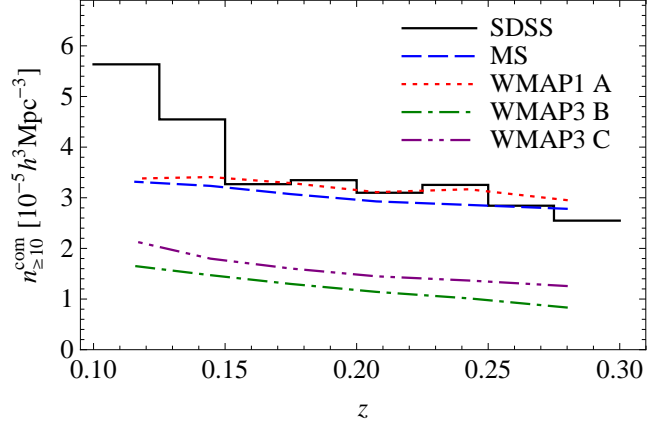


Figure 4. The comoving abundance $n_{\geq 10}^{\text{com}}(z)$ of clusters with richness $N_{200}^{\text{gal}} \geq 10$ as a function of redshift z in the SDSS maxBCG catalogue (Koester et al. 2007a) and in our simulated cluster catalogues based on the MS and the WMAP simulations.

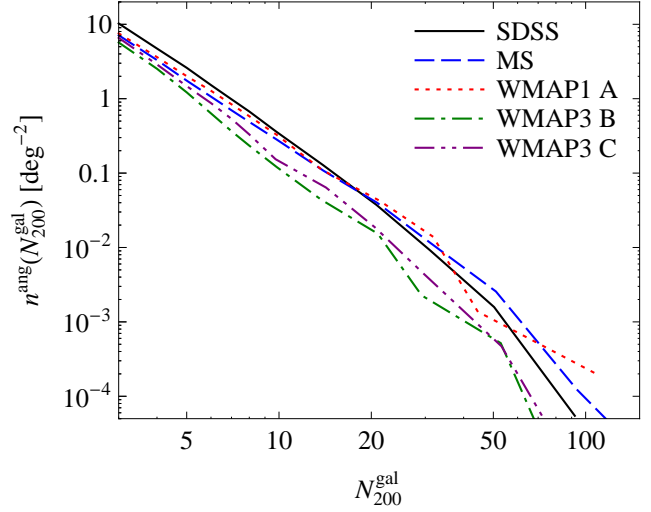


Figure 5. The surface density $n^{\text{ang}}(N_{200}^{\text{gal}})$ of clusters with redshift $0.1 \leq z \leq 0.3$ as a function of richness N_{200}^{gal} . Counts in the SDSS maxBCG cluster sample are compared to counts in our simulated cluster catalogues for the MS and the WMAP simulations.

tions. The differences between the models are largest in the high- N_{200}^{gal} tail of the distribution.

The low cluster abundance for the WMAP3 models in comparison to the MS and WMAP1-A models, in particular for large N_{200}^{gal} , are a reflection of the different cosmologies. Rich clusters have massive dark matter halos, and there are far fewer massive halos in the WMAP3 cosmology than in the WMAP1 cosmology. This is mainly due to the lower value of σ_8 . The higher star formation efficiency in the WMAP3 models does not sufficiently enhance the number of bright ridgeline galaxies per unit mass to compensate for the decrease in the number of massive halos. As a result, there are fewer rich clusters in the WMAP3 models than in the MS and WMAP1-A models.

The observed abundance of rich clusters is much larger than the abundance predicted by the WMAP3 models. This

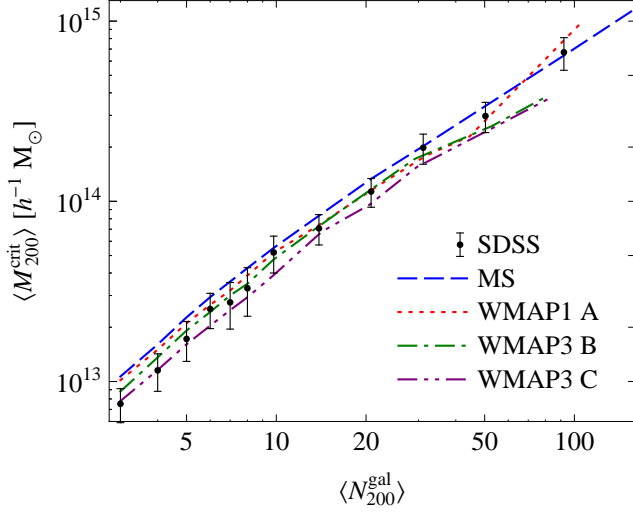


Figure 6. The average cluster mass $\langle M_{200}^{\text{crit}} \rangle$ vs. richness $\langle N_{200}^{\text{gal}} \rangle$ relations for cluster catalogues from the MS and WMAP simulations are compared to the relation derived from the SDSS maxBCG catalogues by Johnston et al. (2007).

suggests that for our Universe σ_8 is closer to 0.9 than to 0.72. This is consistent with some recent estimates (e.g. $\sigma_8 = 0.812 \pm 0.026$ by Komatsu et al. 2009).

3.3 Mass-richness relation

In Fig. 6, average cluster masses $\langle M_{200}^{\text{crit}} \rangle$ in our simulated catalogues are shown as a function of cluster richness $\langle N_{200}^{\text{gal}} \rangle$ and are compared to the corresponding relation for SDSS maxBCG clusters given by Johnston et al. (2007).⁷ Remarkably, all our simulations reproduce the observed mass-richness relation within $\sim 30\%$ over the two orders of magnitude spanned by the SDSS clusters. This corroborates our finding in Sec. 3.1 that our models provide an adequate description of the statistical properties of optically selected galaxy clusters.

At given richness, the differences in cluster density profiles between models and observations (see Fig 3) imply differences in mean cluster mass. For $N_{200}^{\text{gal}} < 10$, the MS yields cluster masses that are 30-40% higher than the SDSS maxBCG cluster masses derived by Johnston et al. (2007). For $N_{200}^{\text{gal}} \geq 10$, the MS masses are up to 20% higher than the SDSS maxBCG masses. The cluster masses of the WMAP1-A model are comparable to those of the MS, but seem to be affected by sampling noise for large $\langle N_{200}^{\text{gal}} \rangle$. The cluster masses in the WMAP3-B model are lower than those for the MS model by 20-30%, and fall below the SDSS cluster masses at large richness. Among our models, the lowest cluster masses are found for the WMAP3-C model, where the values are always smaller than those in the SDSS.

The mass-richness relation for the WMAP1-A model differs by up to 30% from the relation for the MS model (which is much less affected by sampling noise due to its

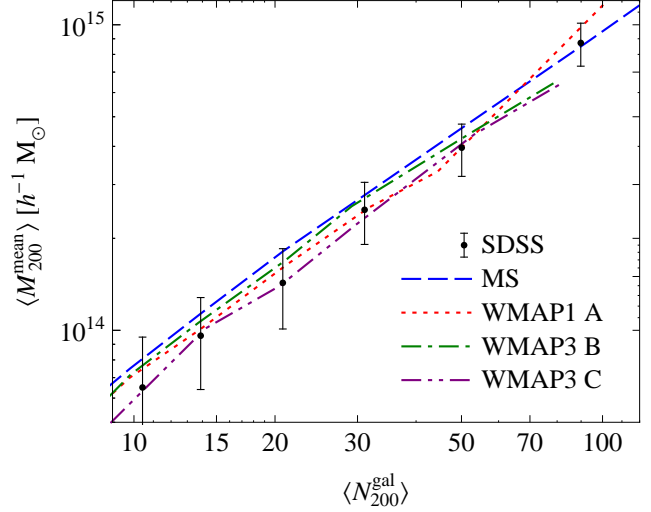


Figure 7. The average cluster mass $\langle M_{200}^{\text{mean}} \rangle$ vs. richness $\langle N_{200}^{\text{gal}} \rangle$ relations for cluster catalogues from our MS and WMAP simulations are compared to the SDSS relation given by Reyes et al. (2008).

Table 4. The best-fit parameters (calculated from a least-squares fit of $\log_{10} \langle N_{200}^{\text{gal}} \rangle$ against $\log_{10} \langle M_{200}^{\text{crit}} \rangle$) for the mass-richness relation (4) of simulated clusters with $N_{200}^{\text{gal}} \geq 9$ is compared to the best-fitting parameters for the SDSS maxBCG clusters with masses measured by Johnston et al. (2007).

	$M_{200 20}^{\text{crit}} [h^{-1} M_{\odot}]$	α_N^{crit}
SDSS	$(1.12 \pm 0.03) \times 10^{14}$	1.14 ± 0.04
MS	$(1.24 \pm 0.01) \times 10^{14}$	1.09 ± 0.01
WMAP1-A	$(1.11 \pm 0.08) \times 10^{14}$	1.21 ± 0.09
WMAP3-B	$(1.05 \pm 0.04) \times 10^{14}$	0.97 ± 0.05
WMAP3-C	$(0.92 \pm 0.04) \times 10^{14}$	1.05 ± 0.05

64 times larger volume). To obtain an estimate for the statistical error on the average cluster masses, we use the MS model to create subsamples with sizes equal to the WMAP1-A model. From these subsamples, we estimate a standard deviation for the binned cluster mass of 2% for $N_{200}^{\text{gal}} = 3$ and 20% for $71 \leq N_{200}^{\text{gal}} \leq 220$. A similar statistical error can be assumed for the WMAP3 models. This is consistent with the differences between the MS and WMAP1-A models being solely due to sampling noise.

Another analysis of the weak-lensing data for the SDSS maxBCG cluster sample has been performed by Reyes et al. (2008). In Fig. 7, we compare the average cluster masses $\langle M_{200}^{\text{mean}} \rangle$ of our simulated clusters to their results as a function of richness. As for $\langle M_{200}^{\text{crit}} \rangle$, the average cluster masses $\langle M_{200}^{\text{mean}} \rangle$ in the MS model are up to 30% larger than the SDSS maxBCG cluster masses, whereas the cluster masses of the WMAP3 models are comparable to those in the SDSS.

The mass-richness relations shown in Fig. 6 and 7 suggest a power law, although with a steeper slope for $\langle N_{200}^{\text{gal}} \rangle < 10$ than for $\langle N_{200}^{\text{gal}} \rangle \gtrsim 10$. Here, we fit the mean mass-richness

⁷ We multiplied the masses given in Johnston et al. (2007) by a factor 1.18 ± 0.06 , which is a photo- z bias correction advocated by Mandelbaum et al. (2008) and Rozo et al. (2008).

Table 5. The best-fit parameters (calculated from a least-squares fit of $\log_{10}\langle N_{200}^{\text{gal}} \rangle$ against $\log_{10}\langle M_{200}^{\text{mean}} \rangle$) for the mass-richness relation (4) of simulated clusters with $N_{200}^{\text{gal}} \geq 9$ is compared to the best-fit parameters for the SDSS maxBCG clusters with masses measured by Reyes et al. (2008).

	$M_{200 20}^{\text{mean}} [h^{-1} \text{M}_{\odot}]$	α_N^{mean}
SDSS	$(1.42 \pm 0.03) \times 10^{14}$	1.19 ± 0.03
MS	$(1.68 \pm 0.02) \times 10^{14}$	1.08 ± 0.01
WMAP1-A	$(1.53 \pm 0.08) \times 10^{14}$	1.19 ± 0.06
WMAP3-B	$(1.58 \pm 0.04) \times 10^{14}$	1.06 ± 0.03
WMAP3-C	$(1.38 \pm 0.04) \times 10^{14}$	1.13 ± 0.04

Table 6. The best-fit parameters for the mass-luminosity relation (5) in our simulations (calculated from a least-squares fit of $\log_{10}\langle L_{200}^{\text{gal}} \rangle$ vs. $\log_{10}\langle M_{200}^{\text{crit}} \rangle$) are compared to the values by Johnston et al. (2007) for the SDSS maxBCG cluster sample.

	$M_{200 40}^{\text{crit}} [h^{-1} \text{M}_{\odot}]$	α_L^{crit}
SDSS	$(1.09 \pm 0.03) \times 10^{14}$	1.23 ± 0.03
MS	$(1.13 \pm 0.02) \times 10^{14}$	1.18 ± 0.01
WMAP1-A	$(1.00 \pm 0.04) \times 10^{14}$	1.16 ± 0.04
WMAP3-B	$(0.89 \pm 0.02) \times 10^{14}$	1.16 ± 0.02
WMAP3-C	$(0.81 \pm 0.02) \times 10^{14}$	1.17 ± 0.02

relation for clusters with $N_{200}^{\text{gal}} \geq 9$ by:

$$M_{200}^{\text{crit/mean}}(N_{200}^{\text{gal}}) = M_{200|20}^{\text{crit/mean}} \left(\frac{N_{200}^{\text{gal}}}{20} \right)^{\alpha_N^{\text{crit/mean}}} \quad (4)$$

The best-fit parameters for our simulated catalogues are compared to those for the SDSS in Tables 4 and 5.

The lower cluster masses in the WMAP3 models than in the MS and WMAP1-A models again reflect the different cosmologies. The less evolved dark matter structure in the WMAP3 cosmology requires more efficient star formation in order to match observed galaxy numbers. This results in more ridgeline galaxies in a dark matter halo of given mass. Consequently, for a given richness, halos are less massive in the WMAP3 models than in the MS and WMAP1-A models.

Except for the largest richness bin, observed cluster masses are smaller than in the MS model. This suggests a normalisation $\sigma_8 < 0.9$ for our Universe (again consistent with the recent estimate $\sigma_8 = 0.812 \pm 0.026$ by Komatsu et al. 2009).

3.4 Mass-luminosity relation

The mass-luminosity relation computed by binning our simulated cluster samples in luminosity L_{200}^{gal} is shown in Fig. 8. For given luminosity, the MS model yields cluster masses very similar to the SDSS masses of Johnston et al. (2007), whereas the WMAP3 model produces mean cluster masses that are generally smaller than the SDSS masses. The best-fit parameters for the mass-luminosity relation

$$M_{200}^{\text{crit}}(L_{200}^{\text{gal}}) = M_{200|40}^{\text{crit}} \left(\frac{L_{200}^{\text{gal}}}{4 \times 10^{11} h^{-2} \text{L}_{\odot}} \right)^{\alpha_L^{\text{crit}}} \quad (5)$$

are listed in Table 6.

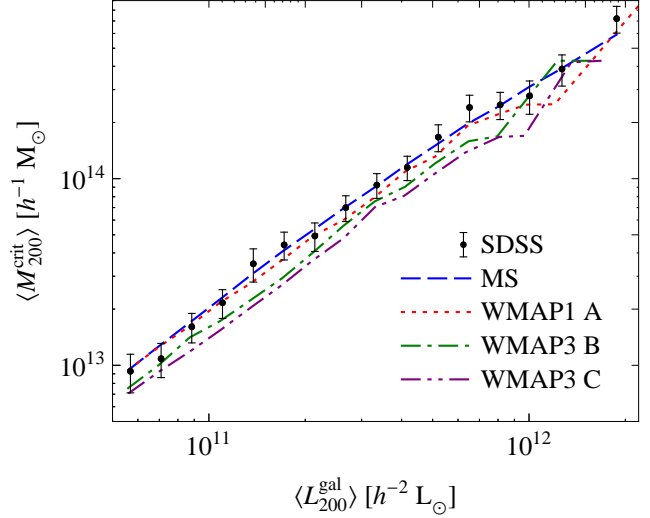


Figure 8. Average cluster mass $\langle M_{200}^{\text{crit}} \rangle$ vs. the total i -band luminosity $\langle L_{200}^{\text{gal}} \rangle$ of ridgeline galaxies within R_{200}^{gal} . Results for our MS and WMAP simulations are compared to SDSS results based on cluster masses by Johnston et al. (2007).

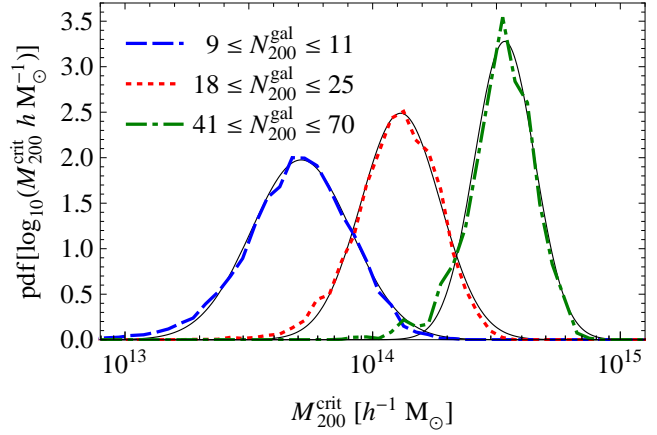


Figure 9. The distribution of the logarithm of cluster mass $\log_{10}(M_{200}^{\text{crit}})$ in various bins of richness N_{200}^{gal} . Shown are distributions for the MS model (dashed/dotted lines) and fits of these distributions to a normal distribution (solid lines).

The differences in the mass-luminosity relation between the various galaxy formation models can be explained in the same way as the differences in the mass-richness relation. The higher star formation efficiency in the WMAP3 models creates more bright ridgeline galaxies in a halo of a given mass M_{200}^{crit} than in the MS and WMAP1-A models. This leads to lower average cluster masses at given luminosity L_{200}^{gal} .

3.5 The scatter in the mass-richness relation

To compute a cluster mass function from cluster counts and mean masses as a function of richness, one needs to model the scatter in mass at each richness. In Fig. 9, distributions of the logarithm of cluster mass $\log_{10}(M_{200}^{\text{crit}})$ are shown for

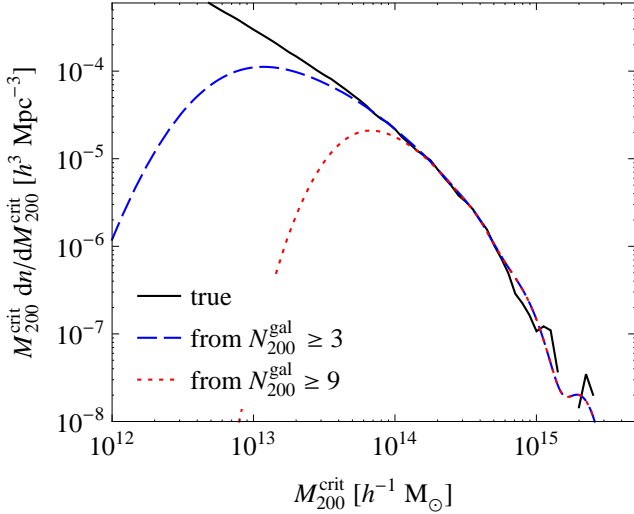


Figure 10. The differential abundance $dn(M_{200}^{\text{crit}})/dM_{200}^{\text{crit}}$ as a function of mass M_{200}^{crit} for clusters with redshift $0.1 \leq z \leq 0.3$ in the MS: directly measured from the simulation (solid line) and reconstructed from the richness bins with $N_{200}^{\text{gal}} \geq 3$ (dashed line) or $N_{200}^{\text{gal}} \geq 9$ (dotted line).

the MS model for several bins in N_{200}^{gal} . These distributions are well described by gaussians.

For our various galaxy formation models, the standard deviation $\sigma_{\log_{10}(M_{200}^{\text{crit}})}$ of the scatter in the logarithm of cluster mass $\log_{10}(M_{200}^{\text{crit}})$ at given N_{200}^{gal} is listed for various N_{200}^{gal} and L_{200}^{gal} -bins in Tables 7-14. The scatter decreases with increasing N_{200}^{gal} or L_{200}^{gal} and tends to be larger at given N_{200}^{gal} than at the corresponding L_{200}^{gal} .

Our values for the scatter in the mass-richness relation are in good agreement with those found empirically by Rozo et al. (2008) for the maxBCG cluster sample (using X-ray luminosities as an additional mass proxy). Moreover, our values are consistent with the scatter in the velocity dispersion-richness relation derived by Becker et al. (2007) for the maxBCG clusters.

3.6 The mass function

When the mass distribution at each richness is known, it is straightforward to reconstruct the cluster mass function (Roza et al. 2008). The differential cluster number density (or differential mass function) is then given by a sum over all richness bins:

$$dn(M_{200}^{\text{crit}})/dM_{200}^{\text{crit}} = \sum_{i=1}^{N_{\text{bins}}} n_i \text{pdf}_i(M_{200}^{\text{crit}}), \quad (6)$$

where n_i denotes the space density and $\text{pdf}_i(M_{200}^{\text{crit}})$ the mass distribution for clusters in richness bin i .

The results of Sec. 3.5 show that the mass distributions $\text{pdf}_i(M_{200}^{\text{crit}})$ at each richness can be approximated by a log-normal distribution with mean $\langle M_{200}^{\text{crit}} \rangle$ and scatter $\sigma_{\log_{10}(M_{200}^{\text{crit}})}$ given by the values in Table 7-10. As Fig. 10 illustrates for the MS model, the reconstructed mass function matches the true mass function well for $M_{200}^{\text{crit}} \gtrsim 2 \times 10^{14}$. For

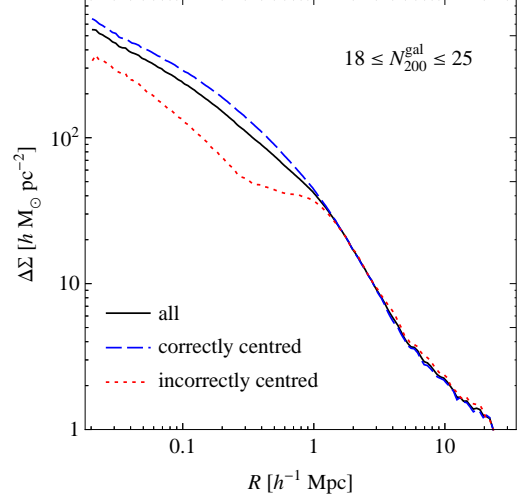


Figure 11. Comparison of the average weak-lensing mass profiles $\Delta\Sigma(R)$ as a function of radius R for all clusters (solid line), for the correctly centred clusters (dashed line), and for the incorrectly centred clusters (dotted line) in the MS.

smaller masses, the richness-selected cluster sample becomes incomplete in mass, and thus the reconstruction fails.

3.7 Fits to the cluster mass profiles

The results of Sec. 3.5 justify the use of a log-normal mass distribution for fits to observed mass profiles (e.g., by Johnston et al. 2007; Reyes et al. 2008). Here, we illustrate that one can indeed obtain a good fit to the simulated mean mass profiles of clusters with assumptions similar to those used, e.g., by Johnston et al. (2007).

The mass profiles discussed in Sec. 3.1 are a mixture of correctly and incorrectly centred clusters. In Fig. 11, the simulated average mass profiles of all clusters are compared to the profiles of correctly and incorrectly centred clusters. The profiles agree well for large radii, but differ significantly below a certain radius $R \approx 0.5 h^{-1}$ Mpc for clusters with richness $N_{200}^{\text{gal}} = 3$, and $R \approx 1 h^{-1}$ Mpc for clusters with $N_{200}^{\text{gal}} \geq 9$.

As Fig. 11 illustrates, centre misidentification has a significant impact on the average cluster mass profiles and thus needs to be taken into account in profile fits. Since stacking weak-lensing mass profiles is linear, we can discuss the contributions from correctly and incorrectly centred clusters separately. A weighted average of fits to these two components constitutes a fit to the average mass profile of all clusters in a richness bin.

We assume that the average mass profile of the correctly centred clusters in a richness bin consists of a central galaxy component, which we model as point mass, a mean dark matter halo modelled as an average over spherical NFW profiles (Navarro et al. 1997), and a contribution from neighbouring mass concentrations. A log-normal distribution with mean $\langle M_{200}^{\text{crit}} \rangle$ and standard deviation $\sigma_{\log_{10}(M_{200}^{\text{crit}})}$ given by Table 7 is assumed for the halo masses. Furthermore, we assume that the concentration c of halos with mass M_{200}^{crit}

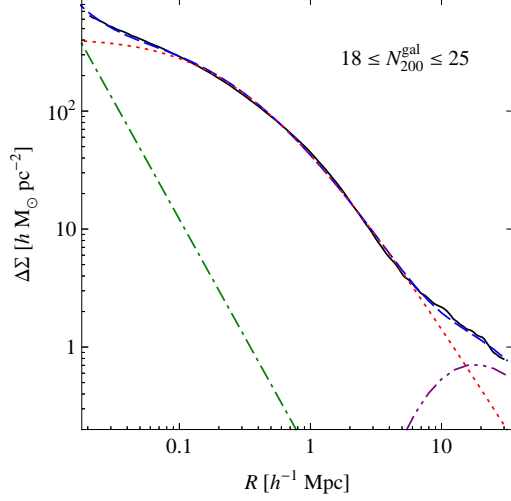


Figure 12. Fit to the weak-lensing mass profile $\Delta\Sigma(R)$ as a function of radius R of correctly centred clusters in the MS model. Shown are the measured profiles (solid line), the 3-component fit (dashed line), the central galaxy contribution (dash dotted line), the DM halo contribution (dotted line), and the contribution from neighbouring masses (dash-dot-dotted line).

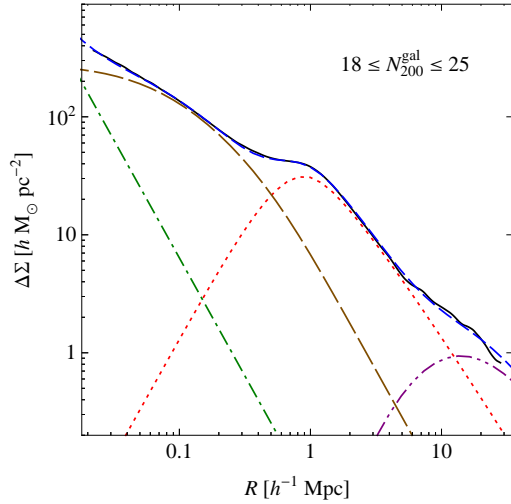


Figure 13. Fit to the weak-lensing mass profile $\Delta\Sigma(R)$ as a function of radius R of incorrectly centred clusters in the MS model. Shown are the measured profiles (solid line), the 4-component fit (short-dashed line), the central galaxy contribution (dash-dotted line), the DM halo contribution (dotted line), the contribution from neighbouring masses (dash-dot-dotted line), and the subhalo contribution (long-dashed line).

follows a log-normal distribution with mean

$$\langle c \rangle (M_{200}^{\text{crit}}) = 4.67 \left(\frac{M_{200}^{\text{crit}}}{10^{14} h^{-1} \text{M}_{\odot}} \right)^{-0.11} \quad (7)$$

and standard deviation $\sigma_{\log_{10}(c)} = 0.15$ (Neto et al. 2007).

The resulting fit to the average weak-lensing mass profile of correctly centred clusters is shown in Fig. 12 for clusters in the MS model with richness $18 \leq N_{200}^{\text{gal}} \leq 25$. A fit of similar quality can also be obtained for the other richness bins.

We now turn to the contribution from incorrectly centred clusters. Figure 11 shows that the average profile of the incorrectly centred clusters increases with decreasing radius even for small radii. This is a consequence of the particular choice for the apparent centre of these clusters in our simulation, namely another massive cluster galaxy within a massive subhalo. If the apparent cluster centres were chosen randomly, one would expect the profile to decrease with decreasing radius for $R < 1 h^{-1} \text{Mpc}$ (Johnston et al. 2007).

To obtain a good fit to the average mass profiles of incorrectly centred clusters, we thus need four components: a central galaxy component (again modelled as point mass), a mean dark matter halo modelled as an NFW profile convolved with a 2D Gaussian, a contribution from neighbouring masses, and a subhalo, which we model as a truncated NFW profile (Baltz et al. 2009). As Fig. 13 illustrates, the subhalo component is essential for a good fit to the simulated mass profiles.

4 SUMMARY AND DISCUSSION

In this work, we have used N -body simulations of cosmic structure formation with semi-analytic galaxy formation modelling to test this modelling and to investigate how the properties of optically selected galaxy groups and clusters depend on cosmological parameters. We have created catalogues of simulated galaxy groups/clusters from model galaxy catalogues (by De Lucia and Blaizot 2007; Wang et al. 2008). We have computed weak-lensing mass profiles and various other properties for these clusters as a function of cluster richness N_{200}^{gal} and luminosity L_{200}^{gal} (as defined by the maxBCG algorithm of Koester et al. 2007b), and compared the results to observations of clusters in the SDSS (Sheldon et al. 2007a; Johnston et al. 2007; Reyes et al. 2008).

We find that the simulated weak-lensing mass profiles and the observed profiles of the SDSS maxBCG clusters agree remarkably well in detailed shape and amplitude. Moreover, all simulations reproduce the observed mass-richness relation within $\sim 30\%$ over the whole range probed by the SDSS clusters. The MS and the WMAP1-A simulation also yield cluster abundances very similar to the observed abundances. This shows that the models considered here provide a good description of the masses, density profiles and optical properties of galaxy clusters as well as the optical cluster selection and richness estimation of the maxBCG algorithm. Evidently, using mock galaxy catalogues based on a large high-resolution Λ CDM structure formation simulation including galaxy formation makes it possible to create very realistic mock cluster catalogues for surveys like the SDSS.

Although the underlying N -body simulations assume different cosmological parameters that lead to different DM halo abundances (Springel et al. 2005; Wang et al. 2008), all the galaxy models used here are able to reproduce the observed abundance and two-point correlations of galaxies reasonably well through careful adjustment of their star-formation efficiency and feedback parameters (De Lucia and Blaizot 2007; Wang et al. 2008). They differ, however, in their predicted cluster abundance as a function of N_{200}^{gal} . The MS model and the WMAP1-A model, both of which

use cosmological parameters based on 1st-year WMAP data (Spergel et al. 2003), predict cluster abundances that are compatible with the observed values (Sheldon et al. 2007a), whereas the WMAP3-A and WMAP3-B models, which use parameters consistent with the WMAP 3rd-year results (Spergel et al. 2007), yield abundances that are lower by a factor 2-3.

The cluster masses predicted as a function of richness N_{200}^{gal} or luminosity L_{200}^{gal} also differ for the different galaxy formation models. At given richness or luminosity, the MS and WMAP1-A models produce clusters that are up to 30% more massive than observed, while the WMAP3 cluster masses are similar to or lower than the observed masses.

The different abundances and average cluster masses in our various galaxy formation models are primarily a reflection of the different underlying cosmologies. Because halos in the WMAP3 cosmology are less massive than in the MS/WMAP1 cosmology, the WMAP3 models need more efficient star formation to match the observed galaxy number densities. This produces more ridgeline galaxies in a dark matter halo of given mass. Consequently, clusters at a given richness are less massive in the WMAP3 models than in the MS and WMAP1-A models. Nevertheless, the higher star formation efficiency in the WMAP3 models does not fully compensate for the lower number of massive halos. So there are fewer rich clusters in the WMAP3 models than in the MS and WMAP1-A models.

Our findings show that cluster abundance and cluster mass as functions of richness can be used directly, in addition to galaxy abundance and two-point statistics, to test galaxy models and to differentiate between cosmologies. The lower cluster masses in the observations compared to the MS model suggests that our Universe would be better described by $\sigma_8 < 0.9$. The higher observed rich cluster abundance than in the WMAP3 models suggests that $\sigma_8 > 0.72$. Thus, more precise agreement between predicted and observed cluster properties is expected for an intermediate value $0.72 < \sigma_8 < 0.9$.

Our results confirm that the mass distribution of clusters of given richness is well described by a log-normal distribution. This justifies both the assumption of such distributions and the specific scatter values adopted in previous work which modelled stacked cluster mass profiles or reconstructed cluster mass functions. Fits to the stacked mass profile of clusters whose centre has erroneously been identified with a non-central cluster galaxy should take into account a halo component associated with this non-central galaxy in addition to its stellar mass, the halo component of the main cluster, and surrounding large-scale structure.

Our simulations required many simplifying assumptions about the richness measurements (e.g. about limiting magnitudes, colours, or projection effects), which could result in biased estimates. Although predictions for cluster abundances or for cluster masses are individually subject to such modelling errors, they do not vary independently for varying assumptions about the richness measurement. For example, assuming a fainter magnitude limit results in lower cluster masses *and* higher cluster numbers. Thus, it proves difficult to decrease average cluster masses for MS model in order to better match the observations without producing too many rich clusters. Similarly, the cluster numbers in the WMAP3 models can only be brought into agreement with the ob-

served counts at the cost of cluster masses which are too small.

In future work, one should test how much the agreement between observed and predicted cluster properties can be improved by choosing different cosmological parameters for the simulations (e.g. the values currently favoured by other observations such as Komatsu et al. 2009). In addition, the galaxy models discussed here should be improved to better match the observed colours of ridgeline galaxies at higher redshift. (If we had not adjusted the ridgeline colour selection by hand, the models would have contained almost no clusters with $z > 0.25$.) Future simulations should also probe other cosmologies and galaxy models. These simulations need to have a much larger volume than the WMAP simulations to have good enough statistics to match upcoming observations. (The statistical errors on the mass-richness relation in the WMAP simulations are comparable to the uncertainties in current observations.)

More realistic modelling of cluster selection and characterisation could be achieved by running the observational cluster-finding algorithms on mock galaxy catalogues created from the simulations. Moreover, ray-tracing techniques could be used to simulate realistically the weak-lensing mass measurements and to assess their statistical accuracy and possible systematic uncertainties.

ACKNOWLEDGMENTS

We thank Gabriella De Lucia, J  r  my Blaizot, Jie Wang, Ben Koester, Erin Sheldon, Jan Hartlap, and Peter Schneider for helpful discussions. We thank Jie Wang and collaborators for granting access to their simulation data. We thank Erin Sheldon for providing the SDSS cluster mass profiles. This work was supported by the DFG within the Priority Programme 1177 under the projects SCHN 342/6 and WH 6/3.

REFERENCES

- Baltz E.A., Marshall P., Oguri M., 2009, *Journal of Cosmology and Astro-Particle Physics*, 1, 15
- Barnes J., White S.D.M., 1984, *MNRAS*, 211, 753
- Bartelmann M., Huss A., Colberg J.M., Jenkins A., Pearce F.R., 1998, *A&A*, 330, 1
- Bartelmann M., Doran M., Wetterich C., 2006, *A&A*, 454, 27
- Becker M.R., et al., 2007, *ApJ*, 669, 905
- Bonaldi A., Tormen G., Dolag K., Moscardini L., 2007, *MNRAS*, 378, 1248
- Borgani S., et al., 2001, *ApJ*, 561, 13
- Colless M., et al., 2003, *VizieR Online Data Catalog*, 7226, 0
- Cooray A., Sheth R., 2002, *Phys. Rep.*, 372, 1
- Croton D.J., et al., 2006, *MNRAS*, 365, 11
- Cypriano E.S., Sodr   L.J., Kneib J.P., Campusano L.E., 2004, *ApJ*, 613, 95
- De Lucia G., Blaizot J., 2007, *MNRAS*, 375, 2
- De Lucia G., Kauffmann G., White S.D.M., 2004, *MNRAS*, 349, 1101

- De Lucia G., Springel V., White S.D.M., Croton D., Kauffmann G., 2006, MNRAS, 366, 499
- Eke V.R., Cole S., Frenk C.S., 1996, MNRAS, 282, 263
- Fedeli C., Bartelmann M., Meneghetti M., Moscardini L., 2008, A&A, 486, 35
- Francis M.J., Lewis G.F., Linder E.V., 2009, MNRAS, 393, L31
- Frenk C.S., White S.D.M., Efstathiou G., Davis M., 1990, ApJ, 351, 10
- Gnedin O.Y., Kravtsov A.V., Klypin A.A., Nagai D., 2004, ApJ, 616, 16
- Grossi M., Springel V., 2008, ArXiv e-prints
- Hansen S.M., McKay T.A., Wechsler R.H., Annis J., Sheldon E.S., Kimball A., 2005, ApJ, 633, 122
- Hoekstra H., 2007, MNRAS, 379, 317
- Jenkins A., Frenk C.S., White S.D.M., Colberg J.M., Cole S., Evrard A.E., Couchman H.M.P., Yoshida N., 2001, MNRAS, 321, 372
- Johnston D.E., et al., 2007, ArXiv e-prints, 709
- Kauffmann G., Colberg J.M., Diaferio A., White S.D.M., 1999, MNRAS, 303, 188
- Kitzbichler M.G., White S.D.M., 2007, MNRAS, 376, 2
- Kochanek C.S., White M., Huchra J., Macri L., Jarrett T.H., Schneider S.E., Mader J., 2003, ApJ, 585, 161
- Koester B.P., et al., 2007a, ApJ, 660, 239
- Koester B.P., et al., 2007b, ApJ, 660, 221
- Komatsu E., et al., 2009, ApJS, 180, 330
- Lukić Z., Heitmann K., Habib S., Bashinsky S., Ricker P.M., 2007, ApJ, 671, 1160
- Mandelbaum R., et al., 2008, MNRAS, 386, 781
- Navarro J.F., Frenk C.S., White S.D.M., 1997, ApJ, 490, 493
- Neto A.F., et al., 2007, MNRAS, 381, 1450
- Piffaretti R., Valdarnini R., 2008, A&A, 491, 71
- Press W.H., Schechter P., 1974, ApJ, 187, 425
- Reiprich T.H., Böhringer H., 2002, ApJ, 567, 716
- Reyes R., Mandelbaum R., Hirata C., Bahcall N., Seljak U., 2008, MNRAS, 390, 1157
- Rines K., Geller M.J., Kurtz M.J., Diaferio A., 2003, AJ, 126, 2152
- Rozo E., et al., 2008, ArXiv e-prints
- Rozo E., et al., 2009, ArXiv e-prints
- Schneider P., Kochanek C., Wambsganss J., 2006, *Gravitational Lensing: Strong, Weak and Micro*, Saas-Fee Advanced Course 33, Springer, Berlin
- Schulz A.E., White M., 2003, ApJ, 586, 723
- Sheldon E.S., et al., 2007a, ArXiv e-prints, 709
- Sheldon E.S., et al., 2007b, ArXiv e-prints, 709
- Sheth R.K., Tormen G., 1999, MNRAS, 308, 119
- Spergel D.N., et al., 2003, ApJS, 148, 175
- Spergel D.N., et al., 2007, ApJS, 170, 377
- Springel V., 2005, MNRAS, 364, 1105
- Springel V., White S.D.M., Tormen G., Kauffmann G., 2001, MNRAS, 328, 726
- Springel V., et al., 2005, Nature, 435, 629
- Stanek R., Evrard A.E., Böhringer H., Schuecker P., Nord B., 2006, ApJ, 648, 956
- Staniszewski Z., et al., 2008, ArXiv e-prints
- Tyson J.A., Wenk R.A., Valdes F., 1990, ApJ, 349, L1
- Vikhlinin A., et al., 2009, ApJ, 692, 1060
- Voit G.M., 2005, Reviews of Modern Physics, 77, 207
- Wambsganss J., Bode P., Ostriker J.P., 2004, ApJ, 606, L93
- Wang J., De Lucia G., Kitzbichler M.G., White S.D.M., 2008, MNRAS, 384, 1301
- Warren M.S., Abazajian K., Holz D.E., Teodoro L., 2006, ApJ, 646, 881
- White M., Hernquist L., Springel V., 2002, ApJ, 579, 16
- Zwicky F., 1937, ApJ, 86, 217

Table 7. The average properties of the model clusters in the MS as inferred from the galaxy model by De Lucia and Blaizot (2007) in bins of richness N_{200}^{gal} : the comoving number density n , the average number $\langle N_{\text{int}}^{\text{gal}} \rangle$ of ridgeline galaxies, the average number $\langle N_{200}^{\text{gal}} \rangle$ of ridgeline galaxies within R_{200}^{gal} , the average cluster radius $\langle R_{200}^{\text{gal}} \rangle$, the average ridgeline i -band luminosity $\langle L_{200}^{\text{gal}} \rangle$ within R_{200}^{gal} , the average cluster masses $\langle M_{200}^{\text{crit}} \rangle$, and the standard deviation $\sigma_{\log_{10}(M_{200}^{\text{crit}})}$ of the logarithmic cluster mass. For bins containing < 7 independent clusters, $\sigma_{\log_{10}(M_{200}^{\text{crit}})}$ is omitted.

bin	N_{200}^{gal}	$n [h^3 \text{Mpc}^{-3}]$	$\langle N_{\text{int}}^{\text{gal}} \rangle$	$\langle N_{200}^{\text{gal}} \rangle$	$\langle R_{200}^{\text{gal}} \rangle [h^{-1} \text{Mpc}]$	$\langle L_{200}^{\text{gal}} \rangle [h^{-1} \text{L}_{\odot}]$	$\langle M_{200}^{\text{crit}} \rangle [h^{-1} \text{M}_{\odot}]$	$\sigma_{\log_{10}(M_{200}^{\text{crit}})}$
1	3	1.2×10^{-4}	2.7	3.0	0.37	5.9×10^{10}	1.1×10^{13}	0.32
2	4	5.6×10^{-5}	3.6	4.0	0.45	8.0×10^{10}	1.6×10^{13}	0.31
3	5	3.0×10^{-5}	4.6	5.0	0.52	1.0×10^{11}	2.3×10^{13}	0.28
4	6	1.8×10^{-5}	5.7	6.0	0.58	1.2×10^{11}	2.9×10^{13}	0.26
5	7	1.2×10^{-5}	6.7	7.0	0.64	1.5×10^{11}	3.6×10^{13}	0.24
6	8	8.3×10^{-6}	7.7	8.0	0.69	1.7×10^{11}	4.3×10^{13}	0.23
7	9-11	1.4×10^{-5}	9.5	9.8	0.78	2.1×10^{11}	5.5×10^{13}	0.21
8	12-17	1.1×10^{-5}	13.7	14.0	0.95	2.9×10^{11}	8.4×10^{13}	0.19
9	18-25	5.4×10^{-6}	20.7	20.9	1.18	4.3×10^{11}	1.3×10^{14}	0.17
10	26-40	3.0×10^{-6}	30.6	31.2	1.44	6.4×10^{11}	2.0×10^{14}	0.15
11	41-70	1.3×10^{-6}	48.9	51.0	1.81	1.0×10^{12}	3.4×10^{14}	0.14
12	71-220	3.3×10^{-7}	86.6	93.8	2.36	1.9×10^{12}	6.6×10^{14}	0.15
13	221-660	1.1×10^{-8}	235.5	269.1	3.69	5.1×10^{12}	2.1×10^{15}	—

Table 8. The properties of the cluster sample in the WMAP1-A model in bins of richness N_{200}^{gal} (see Table 7 for a description of the listed quantities).

bin	N_{200}^{gal}	$n [h^3 \text{Mpc}^{-3}]$	$\langle N_{\text{int}}^{\text{gal}} \rangle$	$\langle N_{200}^{\text{gal}} \rangle$	$\langle R_{200}^{\text{gal}} \rangle [h^{-1} \text{Mpc}]$	$\langle L_{200}^{\text{gal}} \rangle [h^{-1} \text{L}_{\odot}]$	$\langle M_{200}^{\text{crit}} \rangle [h^{-1} \text{M}_{\odot}]$	$\sigma_{\log_{10}(M_{200}^{\text{crit}})}$
1	3	1.3×10^{-4}	2.7	3.0	0.37	6.0×10^{10}	1.0×10^{13}	0.32
2	4	6.2×10^{-5}	3.6	4.0	0.45	8.1×10^{10}	1.5×10^{13}	0.30
3	5	3.4×10^{-5}	4.7	5.0	0.52	1.0×10^{11}	2.1×10^{13}	0.26
4	6	2.2×10^{-5}	5.8	6.0	0.58	1.2×10^{11}	2.7×10^{13}	0.24
5	7	1.4×10^{-5}	6.8	7.0	0.64	1.4×10^{11}	3.2×10^{13}	0.22
6	8	9.9×10^{-6}	7.8	8.0	0.69	1.7×10^{11}	3.9×10^{13}	0.22
7	9-11	1.7×10^{-5}	9.4	9.8	0.77	2.1×10^{11}	5.2×10^{13}	0.22
8	12-17	1.1×10^{-5}	13.5	13.8	0.94	2.9×10^{11}	7.3×10^{13}	0.19
9	18-25	5.8×10^{-6}	22.1	21.3	1.20	4.3×10^{11}	1.2×10^{14}	0.16
10	26-40	3.6×10^{-6}	30.9	31.8	1.46	6.6×10^{11}	1.8×10^{14}	0.16
11	41-70	7.9×10^{-7}	40.2	44.5	1.71	8.9×10^{11}	2.3×10^{14}	—
12	71-220	5.1×10^{-7}	94.4	108.1	2.49	2.1×10^{12}	1.0×10^{15}	—

Table 9. The properties of the cluster sample in the WMAP3-B model in bins of richness N_{200}^{gal} (see Table 7 for a description of the listed quantities).

bin	N_{200}^{gal}	$n [h^3 \text{Mpc}^{-3}]$	$\langle N_{\text{int}}^{\text{gal}} \rangle$	$\langle N_{200}^{\text{gal}} \rangle$	$\langle R_{200}^{\text{gal}} \rangle [h^{-1} \text{Mpc}]$	$\langle L_{200}^{\text{gal}} \rangle [h^{-1} \text{L}_{\odot}]$	$\langle M_{200}^{\text{crit}} \rangle [h^{-1} \text{M}_{\odot}]$	$\sigma_{\log_{10}(M_{200}^{\text{crit}})}$
1	3	9.6×10^{-5}	2.7	3.0	0.37	5.9×10^{10}	8.8×10^{12}	0.33
2	4	4.2×10^{-5}	3.6	4.0	0.44	8.2×10^{10}	1.4×10^{13}	0.33
3	5	2.0×10^{-5}	4.6	5.0	0.51	1.0×10^{11}	1.9×10^{13}	0.29
4	6	1.1×10^{-5}	5.7	6.0	0.58	1.3×10^{11}	2.4×10^{13}	0.27
5	7	6.2×10^{-6}	6.9	7.0	0.64	1.5×10^{11}	3.0×10^{13}	0.26
6	8	3.9×10^{-6}	7.9	8.0	0.70	1.7×10^{11}	3.5×10^{13}	0.24
7	9-11	6.3×10^{-6}	9.8	9.8	0.79	2.2×10^{11}	4.8×10^{13}	0.25
8	12-17	4.7×10^{-6}	14.6	13.7	0.94	3.0×10^{11}	7.2×10^{13}	0.20
9	18-25	2.2×10^{-6}	21.5	21.0	1.18	4.6×10^{11}	1.2×10^{14}	—
10	26-40	6.6×10^{-7}	33.8	29.2	1.36	6.3×10^{11}	1.7×10^{14}	—
11	41-70	3.0×10^{-7}	64.4	52.9	1.74	1.1×10^{12}	2.6×10^{14}	—
12	71-220	1.6×10^{-7}	72.6	80.4	2.03	1.5×10^{12}	3.8×10^{14}	—

Table 10. The properties of the cluster sample in the WMAP3-C model in bins of richness N_{200}^{gal} (see Table 7 for a description of the listed quantities).

bin	N_{200}^{gal}	$n [h^3 \text{Mpc}^{-3}]$	$\langle N_{\text{int}}^{\text{gal}} \rangle$	$\langle N_{200}^{\text{gal}} \rangle$	$\langle R_{200}^{\text{gal}} \rangle [h^{-1} \text{Mpc}]$	$\langle L_{200}^{\text{gal}} \rangle [h^{-1} L_{\odot}]$	$\langle M_{200}^{\text{crit}} \rangle [h^{-1} M_{\odot}]$	$\sigma_{\log_{10}(M_{200}^{\text{crit}})}$
1	3	1.1×10^{-4}	2.6	3.0	0.37	5.8×10^{10}	7.8×10^{12}	0.33
2	4	4.9×10^{-5}	3.6	4.0	0.44	7.9×10^{10}	1.2×10^{13}	0.32
3	5	2.5×10^{-5}	4.6	5.0	0.52	1.0×10^{11}	1.6×10^{13}	0.28
4	6	1.5×10^{-5}	5.6	6.0	0.58	1.2×10^{11}	2.0×10^{13}	0.26
5	7	9.1×10^{-6}	6.5	7.0	0.63	1.4×10^{11}	2.5×10^{13}	0.24
6	8	5.6×10^{-6}	7.3	8.0	0.68	1.7×10^{11}	2.9×10^{13}	0.24
7	9-11	7.9×10^{-6}	9.3	9.7	0.77	2.1×10^{11}	3.9×10^{13}	0.24
8	12-17	6.6×10^{-6}	14.6	14.2	0.97	3.1×10^{11}	6.8×10^{13}	0.19
9	18-25	2.6×10^{-6}	20.4	20.5	1.16	4.3×10^{11}	9.5×10^{13}	0.20
10	26-40	1.2×10^{-6}	30.1	29.6	1.41	6.5×10^{11}	1.5×10^{14}	—
11	41-70	2.5×10^{-7}	65.7	53.2	1.77	1.1×10^{12}	2.5×10^{14}	—
12	71-220	2.7×10^{-7}	77.5	82.0	2.09	1.6×10^{12}	3.7×10^{14}	—

Table 11. The average properties of the model clusters in the MS model in bins of luminosity L_{200}^{gal} (see Table 7 for a description of the listed quantities).

bin	$L_{200}^{\text{gal}} [10^{10} h^{-2} L_{\odot}]$	$n [h^3 \text{Mpc}^{-3}]$	$\langle N_{\text{int}}^{\text{gal}} \rangle$	$\langle N_{200}^{\text{gal}} \rangle$	$\langle R_{200}^{\text{gal}} \rangle [h^{-1} \text{Mpc}]$	$\langle L_{200}^{\text{gal}} \rangle [h^{-1} L_{\odot}]$	$\langle M_{200}^{\text{crit}} \rangle [h^{-1} M_{\odot}]$	$\sigma_{\log_{10}(M_{200}^{\text{crit}})}$
1	5.00 - 6.24	4.1×10^{-5}	2.9	3.3	0.39	5.6×10^{10}	1.0×10^{13}	0.27
2	5.24 - 7.80	4.4×10^{-5}	3.3	3.6	0.42	7.0×10^{10}	1.3×10^{13}	0.27
3	7.80 - 9.74	3.9×10^{-5}	3.8	4.1	0.46	8.7×10^{10}	1.8×10^{13}	0.27
4	9.74 - 12.2	3.1×10^{-5}	4.6	4.9	0.51	1.1×10^{11}	2.4×10^{13}	0.26
5	12.2 - 15.2	2.2×10^{-5}	5.7	5.9	0.58	1.4×10^{11}	3.2×10^{13}	0.24
6	15.2 - 19.0	1.6×10^{-5}	7.2	7.4	0.66	1.7×10^{11}	4.2×10^{13}	0.21
7	19.0 - 23.7	1.1×10^{-5}	9.2	9.3	0.76	2.1×10^{11}	5.6×10^{13}	0.19
8	27.7 - 29.6	7.7×10^{-6}	11.7	11.8	0.87	2.6×10^{11}	7.4×10^{13}	0.18
9	29.6 - 36.9	5.2×10^{-6}	14.9	15.0	0.99	3.3×10^{11}	9.5×10^{13}	0.16
10	36.9 - 46.1	3.7×10^{-6}	18.7	18.9	1.12	4.1×10^{11}	1.2×10^{14}	0.16
11	46.1 - 57.6	2.5×10^{-6}	23.7	23.8	1.26	5.1×10^{11}	1.6×10^{14}	0.15
12	57.6 - 71.9	1.6×10^{-6}	29.3	29.8	1.40	6.4×10^{11}	2.0×10^{14}	0.13
13	71.9 - 89.8	9.6×10^{-7}	37.0	37.9	1.57	8.0×10^{11}	2.6×10^{14}	0.13
14	89.8 - 112.1	6.5×10^{-7}	46.7	47.5	1.76	1.0×10^{12}	3.3×10^{14}	0.12
15	112.1 - 140	4.1×10^{-7}	56.8	59.7	1.94	1.2×10^{12}	4.1×10^{14}	0.13
16	140 - 450	3.6×10^{-7}	84.7	91.2	2.31	1.9×10^{12}	6.4×10^{14}	0.16

Table 12. The average properties of the model clusters in the WMAP1-A model in bins of luminosity L_{200}^{gal} (see Table 7 for a description of the listed quantities).

bin	$L_{200}^{\text{gal}} [10^{10} h^{-2} L_{\odot}]$	$n [h^3 \text{Mpc}^{-3}]$	$\langle N_{\text{int}}^{\text{gal}} \rangle$	$\langle N_{200}^{\text{gal}} \rangle$	$\langle R_{200}^{\text{gal}} \rangle [h^{-1} \text{Mpc}]$	$\langle L_{200}^{\text{gal}} \rangle [h^{-1} L_{\odot}]$	$\langle M_{200}^{\text{crit}} \rangle [h^{-1} M_{\odot}]$	$\sigma_{\log_{10}(M_{200}^{\text{crit}})}$
1	5.00 - 6.24	4.4×10^{-5}	2.9	3.3	0.39	5.6×10^{10}	9.8×10^{12}	0.27
2	5.24 - 7.80	5.0×10^{-5}	3.2	3.6	0.42	7.0×10^{10}	1.3×10^{13}	0.26
3	7.80 - 9.74	4.4×10^{-5}	3.9	4.2	0.46	8.7×10^{10}	1.7×10^{13}	0.26
4	9.74 - 12.2	3.7×10^{-5}	4.7	5.0	0.52	1.1×10^{11}	2.2×10^{13}	0.24
5	12.2 - 15.2	2.5×10^{-5}	5.6	5.9	0.57	1.4×10^{11}	2.8×10^{13}	0.22
6	15.2 - 19.0	1.7×10^{-5}	7.2	7.2	0.65	1.7×10^{11}	3.8×10^{13}	0.21
7	19.0 - 23.7	1.2×10^{-5}	9.1	9.2	0.75	2.1×10^{11}	5.0×10^{13}	0.19
8	27.7 - 29.6	9.3×10^{-6}	11.4	11.5	0.85	2.6×10^{11}	6.6×10^{13}	0.17
9	29.6 - 36.9	5.9×10^{-6}	14.9	14.5	0.97	3.3×10^{11}	8.5×10^{13}	0.17
10	36.9 - 46.1	4.3×10^{-6}	21.0	19.8	1.15	4.1×10^{11}	1.1×10^{14}	0.15
11	46.1 - 57.6	2.5×10^{-6}	22.8	24.0	1.26	5.1×10^{11}	1.3×10^{14}	–
12	57.6 - 71.9	1.4×10^{-6}	29.2	30.4	1.42	6.5×10^{11}	1.8×10^{14}	–
13	71.9 - 89.8	1.7×10^{-6}	36.2	37.6	1.59	8.0×10^{11}	2.2×10^{14}	–
14	89.8 - 112.1	3.9×10^{-7}	39.4	43.5	1.65	9.6×10^{11}	2.3×10^{14}	–
15	112.1 - 140	1.8×10^{-7}	55.0	63.9	1.88	1.2×10^{12}	2.3×10^{14}	–
16	140 - 450	5.1×10^{-7}	94.5	108.1	2.50	2.1×10^{12}	1.0×10^{15}	–

Table 13. The average properties of the model clusters in the WMAP3-B model in bins of luminosity L_{200}^{gal} (see Table 7 for a description of the listed quantities).

bin	$L_{200}^{\text{gal}} [10^{10} h^{-2} L_{\odot}]$	$n [h^3 \text{Mpc}^{-3}]$	$\langle N_{\text{int}}^{\text{gal}} \rangle$	$\langle N_{200}^{\text{gal}} \rangle$	$\langle R_{200}^{\text{gal}} \rangle [h^{-1} \text{Mpc}]$	$\langle L_{200}^{\text{gal}} \rangle [h^{-1} L_{\odot}]$	$\langle M_{200}^{\text{crit}} \rangle [h^{-1} M_{\odot}]$	$\sigma_{\log_{10}(M_{200}^{\text{crit}})}$
1	5.00 - 6.24	3.0×10^{-5}	2.8	3.3	0.39	5.6×10^{10}	8.5×10^{12}	0.29
2	5.24 - 7.80	3.2×10^{-5}	3.2	3.6	0.41	7.0×10^{10}	1.1×10^{13}	0.29
3	7.80 - 9.74	3.0×10^{-5}	3.8	4.0	0.45	8.7×10^{10}	1.5×10^{13}	0.29
4	9.74 - 12.2	2.1×10^{-5}	4.4	4.6	0.49	1.1×10^{11}	1.9×10^{13}	0.27
5	12.2 - 15.2	1.4×10^{-5}	5.3	5.4	0.54	1.4×10^{11}	2.4×10^{13}	0.26
6	15.2 - 19.0	8.9×10^{-6}	6.8	6.8	0.63	1.7×10^{11}	3.3×10^{13}	0.24
7	19.0 - 23.7	5.1×10^{-6}	8.9	8.7	0.74	2.1×10^{11}	4.2×10^{13}	0.22
8	27.7 - 29.6	3.7×10^{-6}	11.2	10.8	0.83	2.6×10^{11}	5.9×10^{13}	0.22
9	29.6 - 36.9	2.6×10^{-6}	14.0	13.6	0.93	3.3×10^{11}	7.5×10^{13}	–
10	36.9 - 46.1	1.8×10^{-6}	18.4	17.5	1.06	4.1×10^{11}	1.0×10^{14}	–
11	46.1 - 57.6	9.6×10^{-7}	25.5	22.2	1.22	5.1×10^{11}	1.4×10^{14}	–
12	57.6 - 71.9	5.0×10^{-7}	30.2	26.2	1.32	6.4×10^{11}	1.6×10^{14}	–
13	71.9 - 89.8	2.6×10^{-7}	43.8	35.4	1.45	7.9×10^{11}	2.1×10^{14}	–
14	89.8 - 112.1	1.5×10^{-7}	59.7	49.1	1.68	1.0×10^{12}	2.3×10^{14}	–
15	112.1 - 140	1.3×10^{-7}	67.9	61.4	1.85	1.2×10^{12}	2.9×10^{14}	–
16	140 - 450	1.4×10^{-7}	72.6	81.3	2.03	1.5×10^{12}	3.8×10^{14}	–

Table 14. The average properties of the model clusters in the WMAP3-C model in bins of luminosity L_{200}^{gal} (see Table 7 for a description of the listed quantities).

bin	$L_{200}^{\text{gal}} [10^{10} h^{-2} \text{L}_{\odot}]$	$n [h^3 \text{Mpc}^{-3}]$	$\langle N_{\text{int}}^{\text{gal}} \rangle$	$\langle N_{200}^{\text{gal}} \rangle$	$\langle R_{200}^{\text{gal}} \rangle [h^{-1} \text{Mpc}]$	$\langle L_{200}^{\text{gal}} \rangle [h^{-1} \text{L}_{\odot}]$	$\langle M_{200}^{\text{crit}} \rangle [h^{-1} \text{M}_{\odot}]$	$\sigma_{\log_{10}(M_{200}^{\text{crit}})}$
1	5.00 - 6.24	3.9×10^{-5}	2.9	3.3	0.39	5.6×10^{10}	8.1×10^{12}	0.29
2	5.24 - 7.80	3.9×10^{-5}	3.3	3.6	0.42	7.0×10^{10}	1.0×10^{13}	0.30
3	7.80 - 9.74	3.3×10^{-5}	3.8	4.1	0.46	8.7×10^{10}	1.3×10^{13}	0.29
4	9.74 - 12.2	2.6×10^{-5}	4.5	4.8	0.50	1.1×10^{11}	1.7×10^{13}	0.27
5	12.2 - 15.2	1.6×10^{-5}	5.5	5.9	0.56	1.4×10^{11}	2.2×10^{13}	0.24
6	15.2 - 19.0	1.0×10^{-5}	6.7	7.0	0.63	1.7×10^{11}	2.9×10^{13}	0.23
7	19.0 - 23.7	6.2×10^{-6}	8.8	8.8	0.73	2.1×10^{11}	3.8×10^{13}	0.21
8	27.7 - 29.6	4.7×10^{-6}	11.6	11.7	0.86	2.6×10^{11}	5.3×10^{13}	0.20
9	29.6 - 36.9	3.5×10^{-6}	14.9	15.0	0.99	3.3×10^{11}	6.9×10^{13}	0.17
10	36.9 - 46.1	2.1×10^{-6}	18.3	17.9	1.09	4.1×10^{11}	9.3×10^{13}	—
11	46.1 - 57.6	1.1×10^{-6}	23.3	23.2	1.24	5.1×10^{11}	1.3×10^{14}	—
12	57.6 - 71.9	6.4×10^{-7}	31.2	27.9	1.38	6.4×10^{11}	1.5×10^{14}	—
13	71.9 - 89.8	3.7×10^{-7}	37.9	33.9	1.49	7.8×10^{11}	1.8×10^{14}	—
14	89.8 - 112.1	1.4×10^{-7}	57.8	48.0	1.70	1.0×10^{12}	2.2×10^{14}	—
15	112.1 - 140	1.4×10^{-7}	67.5	59.7	1.87	1.2×10^{12}	2.7×10^{14}	—
16	140 - 450	2.8×10^{-7}	77.3	81.1	2.07	1.6×10^{12}	3.7×10^{14}	—